# Phosphorus-Doped Silicon Nanocrystals Exhibiting Mid-Infrared Localized Surface Plasmon Resonance

David J. Rowe,[†] Jong Seok Jeong,[‡] K. Andre Mkhoyan,[‡] and Uwe R. Kortshagen[*,†]

[†]Department of Mechanical Engineering and [‡]Department of Chemical Engineering and Materials Science, University of Minnesota, Minneapolis, Minnesota 55455, United States

**S** *Supporting Information*

**ABSTRACT:** Localized surface plasmon resonances (LSPRs) enable tailoring of the optical response of nanomaterials through their free carrier concentration, morphology, and dielectric environment. Recent efforts to expand the spectral range of usable LSPR frequencies into the infrared successfully demonstrated LSPRs in doped semiconductor nanocrystals. Despite silicon's importance for electronic and photonic applications, no LSPRs have been reported for doped silicon nanocrystals. Here we demonstrate doped silicon nanocrystals synthesized via a nonthermal plasma technique that exhibits tunable LSPRs in the energy range of 0.07−0.3 eV or mid-infrared wavenumbers of 600−2500 cm$^{-1}$.



**KEYWORDS:** *Silicon nanocrystals, localized surface plasmon resonance, doping*
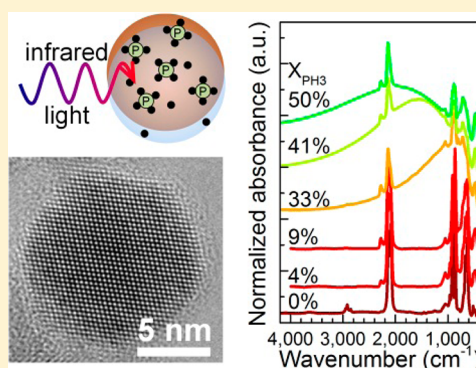
A localized surface plasmon resonance (LSPR) describes the collective oscillation of free charge carriers, which are dielectrically confined in a nanoparticle in response to an external electromagnetic field.[1] Nanoparticles exhibiting LSPR display remarkable light scattering and absorption properties, stimulating intense research due to their applications in biosensing,[2] spectroscopy enhancement,[3] subwavelength microscopy,[4] and photovoltaics.[5] Among plasmonic materials, noble metals receive significant attention owing to their large free charge carrier concentration, $N_{fc} \sim 10^{22}-10^{23}$ cm$^{-3}$, resulting in resonances within the visible spectral range.[1] However, recent efforts are exploring the potential of heavily doped semiconductor nanocrystals (NCs) for LSPRs in the infrared spectral range.[6−10] Despite silicon's importance for electronic and photonic applications, no LSPRs have been reported for doped silicon NCs (SiNCs). Chou et al.[11] identified a surface plasmon associated with doped nanowires, however tunability was accomplished through manipulation of the length of the nanowire and the effect of the doping concentration was not explored. Here we show degenerately doped SiNCs synthesized via a one-step nonthermal plasma technique exhibit tunable LSPRs in the energy range of 0.07−0.3 eV, or mid-infrared wavenumbers of 600−2500 cm$^{-1}$.

LSPRs enable one to tailor the optical response of nanomaterials through $N_{fc}$, morphology, and dielectric environment. However, unlike in metals $N_{fc}$ in semiconductors can be tailored by tuning the doping concentration or by other parameters such as temperature and/or charge injection, potentially enabling dynamic control of the LSPR response.[12,13] The lower $N_{fc}$ in semiconductors ($10^{18}-10^{21}$ cm$^{-3}$) shift LSPR frequencies into the near-infrared (NIR) through the terahertz

(THz) region. The scarcity of tunable optical materials in this region is referred to as the "THz gap" in photonics, causing THz technology to develop slowly.[14] Unfortunately, effectively doping semiconductor NCs remains far from trivial. Dopant segregation to the NC surface may severely reduce the dopants' ability to provide free charge carriers.[15] At high synthesis temperatures, "self-purification" may occur, as NCs expel dopant atoms to the surface to lower the NCs' free energy.[16] At lower temperature, dopant incorporation requires favorable surface conditions for dopant atoms to attach and be covered by additional atoms before becoming embedded in the NC.[17] Both processes may impose upper limits for $N_{fc}$ and limit the potential of some semiconductors to display LSPRs. Vacancy doping elegantly circumvents some problems associated with impurity doping in compound semiconductors;[6−9] however, in group IV NCs, free charge carriers are generally not formed through vacancies,[18,19] thereby requiring substitutional doping.

In Figure 1a,b, we examine the conditions under which mid-IR LSPRs in phosphorus-doped SiNCs may show expected resonant frequencies, following the analysis by Luther et al.[6] (Supporting Information Section S-1). Luther et al. suggested that <10 carriers per 10 nm NC may be insufficient to support LSPRs,[6] placing a lower limit for $N_{fc}$ in SiNCs at $1 \times 10^{19}$ cm$^{-3}$ with ~0.02 atom % of dopant. Electrically activated phosphorus (P) concentrations in Si strongly depend on the activation process, giving a range for the upper limit of $N_{fc}$. Nobili et al.[20]
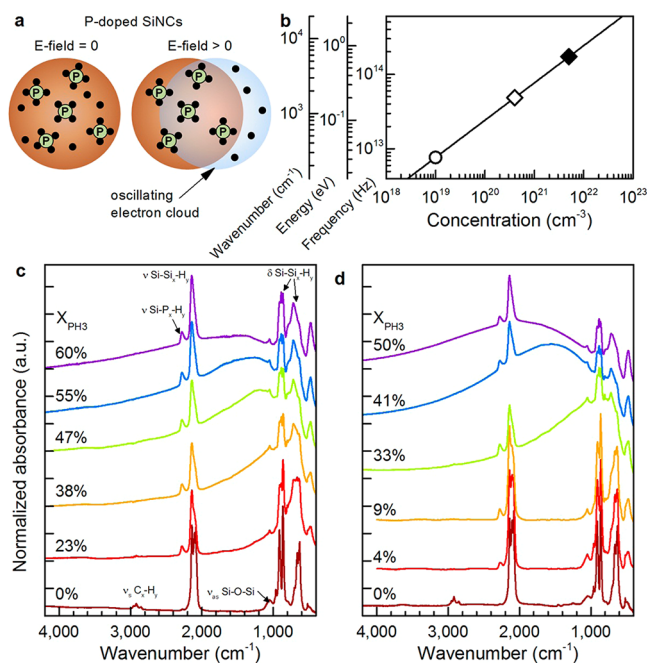
**Figure 1.** LSPR from P-doped SiNCs. (a) Schematic of P-doped SiNC exhibiting LSPR under an applied electric field. The LSPR mode is supported by donated electrons from electrically active P atoms. (b) LSPR frequency, $f_{LSPR}$, for a spherical nanoparticle of subwavelength diameter, neglecting scattering estimated from the free charge carrier concentration, $N_{fc}$, by $f_{LSPR} = (1/2\pi)((N_{fc}e^2)/(\varepsilon_o m_e^*(\varepsilon_\infty + 2\varepsilon_m)))^{1/2}$, where $e$ is the electronic charge, $m_e^*$ is the free carrier effective mass taken as rest mass of a free electron ($m_e^*/m_o \sim 1$), $\varepsilon_o$ is the free space permittivity, $\varepsilon_\infty$ is the high frequency dielectric constant assumed to be that of bulk Si (11.7), and $\varepsilon_m$ is the medium dielectric constant, assumed here to be 1 for a nitrogen atmosphere. Conversion to wavenumber and energy are included for reference. Symbols identify the lower limit of $N_{fc}$ given by ref 6 (circle) and the upper limits given by ref 19 for laser annealed (filled diamond) and thermally annealed (open diamond) P-doped Si samples. (c,d) Normalized FTIR spectra of P-doped SiNCs for a range of $X_{PH3}$ for two different synthesis pressures, $P = 113$ and 206 Pa, respectively. As $X_{PH3}$ increases, a broad absorption feature develops and blue shifts. Relevant surface vibrations are also identified as sharper features superimposed on the broad absorption. Assignment of Si surface vibrational modes can be found in the Supporting Information Section S-3. Spectra are offset vertically for clarity.

measured $N_{fc}$ as high as $5 \times 10^{21}$ cm$^{-3}$ with ~10 atom % of dopant for ion-implanted Si annealed with a pulsed laser and showed that $N_{fc}$ decreased to $4 \times 10^{20}$ cm$^{-3}$ with 0.8 atom % of dopant when subsequently annealed at 1273 K for 5 min. Pi et al.[21] achieved doping concentrations in SiNCs in the 0.1−10 atom % range with nonthermal plasma synthesis, as first proposed by Mangolini et al.[22] We adapted the synthesis technique from Pi et al. for this work (see Methods for full description of synthesis and characterization). Pi et al.[21] pointed out that P is taken up by the SiNC core with approximately 10−20% efficiency using a silane/phosphine ([SiH$_4$]/[PH$_3$]) plasma. Hence, it is reasonable to expect that a fractional PH$_3$ flow rate, defined as $X_{PH3} = $[PH$_3$]/([PH$_3$] + [SiH$_4$]) × 100%, on the order of several 10% is required to achieve LSPR from SiNCs. For bulk Si, such large $X_{PH3}$ appears unreasonably high, likely deterring such conditions for SiNC production and explaining the lack of LSPR observations in SiNCs.[21,23−26]

Figure 1c,d show the IR absorption spectra of samples produced with varying $X_{PH3}$ for two different pressures in the plasma reactor. In Figure 1c, a broad absorption consistent with LSPR shifts from 400 to 1500 cm$^{-1}$ as $X_{PH3}$ increases, superimposed with surface vibrational modes (assignments in Supporting Information Section S-2). Additionally, a small peak at 2276 cm$^{-1}$ grows with increasing $X_{PH3}$ attributable to Si−P$_x$-H$_y$ surface vibrations,[27] consistent with increasing P segregation at the SiNC surface. As shown in Figure 1d, P-doped SiNCs produced at a higher pressure display LSPRs varying controllably through 600−2000 cm$^{-1}$. However, $X_{PH3}$ required for the same blue shift as in Figure 1c is reduced, indicating a larger $N_{fc}$ in these samples. Additional data confirm a shift of the broad absorption with changes in the dielectric environment, consistent with an LSPR mode (Supporting Information Section S-3). To our knowledge, this is the first observation of tunable LSPRs in impurity doped SiNCs.

Performing SiNC synthesis under $X_{PH3}$ as high as 60% is unprecedented and thus calls for detailed materials characterization as unwanted stable silicon phosphides may form as synthesis byproducts and degrade the doping effectiveness. Figure 2a−f shows transmission electron microscopy (TEM) images and size histograms for undoped, lightly doped, and heavily doped SiNCs ($X_{PH3} = 0$, 8.2, and 47 atom %, respectively). Bright-field (BF) TEM images reveal that particles have a crystalline core with approximately a 1 nm
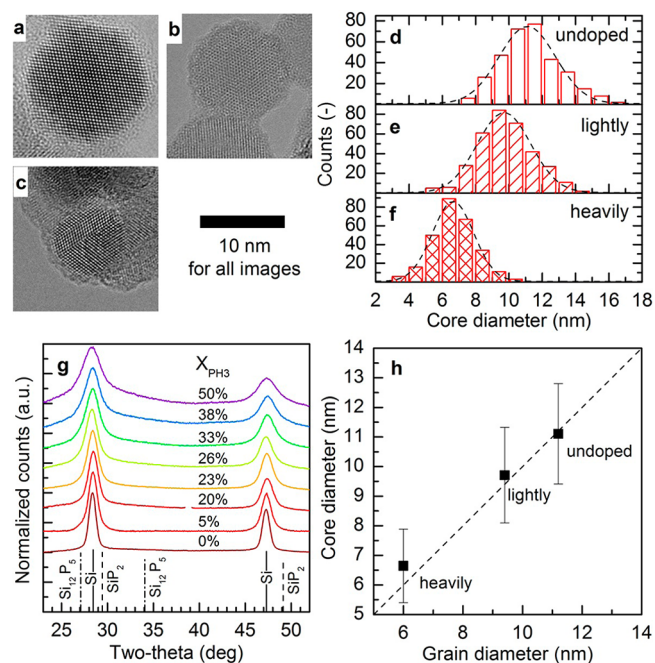


**Figure 2.** P-doped SiNC crystal structure. (a−c) BF-TEM images of SiNCs and (d−f) corresponding histograms for core diameters of undoped, lightly, and heavily P-doped SiNCs ($X_{PH3} = 0$, 8.2, and 47%, respectively). Mean core diameter is estimated from a Gaussian fit to the histogram data (dashed line). (g) XRD patterns of SiNCs with increasing $X_{PH3}$ indicate that diamond cubic Si is the only phase present. Diffraction patterns are offset vertically for clarity, and the angles for reflections from Si−P compounds are included for comparison. (h) Comparison between the grain diameter measured by XRD and the core diameter measured by TEM. The dashed line indicates 1:1 agreement between two measurement techniques. Error bars specify the standard deviation from Gaussian fits of the histograms shown in (d−f).
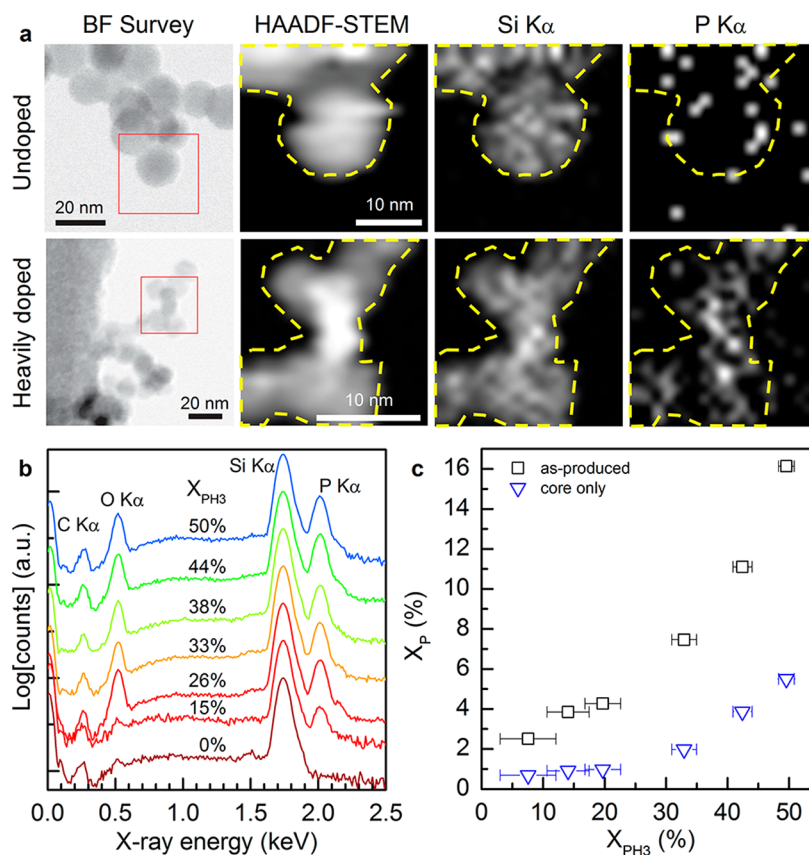
**Figure 3.** P incorporation in SiNCs. (a) BF-TEM images for survey, high-angle annular dark field (HAADF) STEM images and corresponding EDX maps for Si K$\alpha$ and P K$\alpha$ lines for undoped and heavily P-doped SiNCs. The red boxes indicate the analysis area. (b) Semilog plot of SEM-EDX spectra for varying $X_{PH3}$ of "as-produced" SiNCs, with C, O, Si, and P K$\alpha$ lines identified at 0.277, 0.525, 1.74, and 2.01 keV, respectively. Oxygen and carbon contamination are estimated at less than 3 atom % and are the result of air exposure during sample transfer. Spectra are offset vertically for clarity. (c) Estimated $X_P$ from SEM-EDX spectra for "as produced" samples (squares) and for samples after surface P had been removed to probe the SiNC core (inverted triangles).

thick amorphous shell, regardless of $X_{PH3}$. Interestingly, samples produced under high $X_{PH3}$ display increased twinning grain boundaries (Supporting Information Section S-4). In Figure 2g, X-ray diffraction (XRD) patterns further confirm the exclusive presence of Si by the absence of higher order diffraction peaks from Si–P compounds. We attribute the diffraction peak broadening as $X_{PH3}$ increases to a decrease in SiNC diameter, consistent with TEM data. Figure 2h compares the NC diameter as derived from TEM images (core diameter) with the diameter derived from XRD data (grain diameter). Though twinning leads to a slight underestimation of particle size with XRD, both diagnostics show good agreement and reveal that the NC size strongly decreases with increasing $X_{PH3}$. This size decrease likely results from the PH$_3$ delivery in a 15:85 dilution in hydrogen, which reduces the NC growth rate through in situ etching.[28] Furthermore, smaller SiNCs and grain boundaries from twinning result in an increasing number of plasmon scattering interfaces, explaining the observed LSPR broadening at large $X_{PH3}$ in Figures 1c,d.[6]

Though Figure 2 indicates that the SiNCs consist only of diamond cubic Si, additional studies were carried out to explore the magnitude and distribution of P within the SiNCs. Figure 3a highlights the results of scanning TEM (STEM) imaging with energy-dispersive X-ray spectroscopy (STEM-EDX) measurements, and suggests that P is either incorporated into the SiNCs and/or condensed on the SiNC surfaces. However, the presence of surface Si–P$_x$–H$_y$ vibrations shown in Figures

1c,d indicates significant P segregation at the surface. In order to probe the atomic P concentration, $X_P = [P]/([P] + [Si]) \times 100\%$, in the SiNC core, we adapted a technique previously used in ref 20, where $X_P$ is measured before and after wet chemical etching of P incorporated in a native oxide shell allowed to form on the SiNCs (detailed process found in Methods). Figure 3b shows the scanning electron microscopy EDX (SEM-EDX) spectra measured for "as-produced" SiNCs with varying $X_{PH3}$. After converting the raw intensity spectra to atomic percentage, $X_P$ shown in Figure 3c suggests 60–75% of P was condensed on the NC surface. To put the P concentration into perspective, we can estimate the number of atoms in a spherical SiNC using simple geometrical arguments. For a SiNC produced at $X_{PH3} \sim 50\%$ we find that core $X_P \sim 5\%$ and from XRD we measure a NC diameter of ~6.5 nm. Therefore, we estimate the NC consists of approximately 7200 atoms, ~350 of which are P. We calculate the overall conversion efficiency of the gaseous PH$_3$ precursor to core P incorporation of ~10%, consistent with previous studies.[21,23] By removing electrically inactive surface P and considering core P, we have attempted to identify a better measure of the electrically activated donor concentration within the SiNC. Nevertheless, atomic concentration measurements will need to be corroborated with electrical transport measurements to further elucidate the true free carrier concentration.
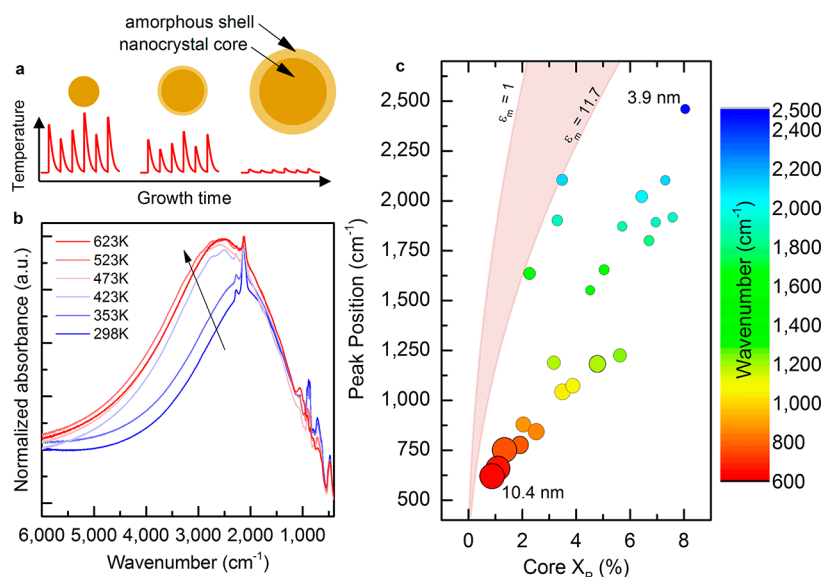
**Figure 4.** Electrically active donors producing free carriers in SiNC core. (a) Schematic describing the mechanism of selective nanoparticle heating. When the SiNC is small, the thermal capacitance is low, and stochastically occurring surface reactions cause large fluctuations in the particle temperature. As the particle grows the temperature fluctuations decrease and thermal energy available for dopant activation decreases. (b) Blue shift of highly P-doped SiNCs upon subsequent low-temperature annealing procedures. (c) Summarized LSPR data for several P-doped SiNC samples as a function of core $X_P$. For emphasis, the bubble size indicates the diameter of the SiNC core and the color corresponds to peak LSPR frequency. The largest and smallest NC diameter, 10.4 and 3.9 nm, respectively, are labeled for reference. The predicted LSPR frequency range formed by assuming $\varepsilon_m = 1$ (nitrogen) and $\varepsilon_m = 11.7$ (Si) are shown for reference. If the dielectric constant of the medium is taken as that of nitrogen ($\varepsilon_m = 1$) the observed LSPR frequencies are significantly lower than the predicted frequencies. However, in a powder samples, the nearby SiNCs likely need to be accounted for in the dielectric constant of the medium. When Si ($\varepsilon_m = 11.7$) is used for a medium the observed shift of the LSPR peak is more consistent with the expected square root dependence on $N_{fc}$.

To understand the NC doping process in a nonthermal plasma, it is important to realize that nanoparticles are selectively heated to temperatures far exceeding the gas temperature by the combination of energetic surface reactions and slow convective cooling in the low-pressure environment.[29] Excursions from an average temperature are more pronounced for smaller nanoparticles, as fewer atoms absorb the energy released by stochastically occurring surface reactions, shown schematically in Figure 4a. When SiNCs are small and intermittently achieve high temperatures, Si atoms easily arrange to form crystalline cores. As the SiNCs grow, the thermal energy available for diffusion decreases, resulting in increased defect formation as Si and P atoms randomly attach to the NC surface. This may explain the amorphous shell observed in TEM in Figure 2a–c, which cannot be explained completely as an oxide layer (see Supporting Information Section S-5). Based on this picture, we hypothesize that some carriers may be trapped in dangling bond defect states near the shell/core interface and do not participate in the LSPR. Recently, low-temperature annealing of SiNCs (<473 K) has proven sufficient for reducing dangling bond defect concentrations by an order of magnitude.[30] As shown in Figure 4b, when we annealed P-doped SiNCs, a clear LSPR blue shift occurs at temperatures as low as 423 K, consistent with an increase in $N_{fc}$ from $6.2 \times 10^{20}$ cm$^{-3}$ to $1.05 \times 10^{21}$ cm$^{-3}$ according to Figure 1b. Because these measurements were recorded at room temperature, we can neglect any contribution from thermally excited carriers, and because the annealing temperatures are much lower than anything reported for electrical activation of P in Si we assume that very few "new" free carriers are generated. Instead, we believe the reduction of dangling bond defects via low temperature annealing actually liberates trapped free carriers from the dangling bonds. Thus,

the SiNC temperature history dramatically impacts the free carrier density. Similarly, since elevated pressures generally lead to increased particle heating in a plasma due to the increased rate of surface reactions, this model also explains the blue shift observed for samples shown in Figures 1c,d.

Figure 4c summarizes the results of this study. It displays the measured LSPR peak positions versus the P concentration in the SiNC core. Predicted LSPR frequencies are shown for the measured P concentrations, ranging between environments with effective medium dielectric constants of nitrogen ($\varepsilon_m = 1$) and Si ($\varepsilon_m = 11.7$). However, these predictions are expected to overestimate the LSPR frequencies due to three likely inaccurate assumptions inherent to the model: (1) all core P is electrically activated and there are no trapped carriers, which likely overestimates $N_{fc}$, (2) interfacial scattering is negligible, and (3) interparticle plasmon coupling, which has been observed in measurements of gold nanoparticles,[31] between nearby SiNCs is ignored. Each of these assumptions contribute to our model predicting a larger LSPR frequency than may be found in our SiNCs, consistent with the data presented in Figure 4c.

In conclusion, all results presented here are consistent with the first observation of LSPR in substitutionally P-doped SiNCs. We have shown that very large $X_{PH3}$ is required during plasma synthesis to produce sufficient electrically activated free carriers for supporting LSPR modes. Furthermore, SiNCs produced under these conditions using the nonthermal plasma synthesis retain a diamond-cubic structure despite large concentrations of P. This facile synthesis approach allows for LSPR tunability in the mid-IR region and may enable silicon-compatible IR photonics at the nanoscale.

**Methods.** *P-Doped SiNC Synthesis and Collection.* The synthesis of highly crystalline, spherical SiNCs is detailed

elsewhere.[22] Briefly, to synthesize heavily P-doped SiNCs, $PH_3$ gas, diluted to 15% in hydrogen for safety reasons, is introduced into an RF capacitively coupled nonthermal argon/$SiH_4$ plasma, operating at a nominal power of 110−130 W. Typical flow rates are 0.5 standard cubic centimeters per minute (sccm) of $SiH_4$, 17 sccm of argon, and 0−4 sccm of $PH_3$ diluted to 15% in hydrogen. A key parameter in this synthesis is the fractional $PH_3$ flow rate, defined as $X_{PH3} = [PH_3]/([PH_3] + [SiH_4] \times 100\%$, and is varied by changing the $PH_3$ flow rate while maintaining constant argon and $SiH_4$ flow rates. Powder samples of P-doped SiNCs are collected directly from the gas-phase by impacting onto a clean substrate mounted onto a manual feed-through located inside the reactor. Impaction is achieved by throttling the gas flow with a convergent, rectangular nozzle. Collisions with the accelerating gas flow transfer momentum to the SiNCs that then travel ballistically until they impact on the substrate. The substrate is placed in the path of the particle beam exiting the nozzle for a specified collection time. The feed-through is then retracted into a portable loadlock and transferred air-free to a nitrogen-purged glovebox for further characterization and processing. In addition to accelerating the SiNCs, the rectangular nozzle controls the gas pressure in the plasma region by restricting flow. By adjusting the width of the nozzle opening, the pressure changes independently of the argon gas flow. This method is used to produce samples at reactor pressures of 113 and 206 Pa. During the synthesis process, an amorphous layer of Si grows on the inner surface of the glass tube where $SiH_4$ dissociation occurs. Only when a clean, fresh tube is used are undoped SiNCs fabricated, suggesting that dopant that is incorporated in the amorphous film can be redistributed among SiNCs when no additional $PH_3$ gas is added. Tubes are cleaned between runs using a potassium hydroxide bath to remove any grown Si films.

*SiNC Characterization.* FTIR measurements are performed using a Bruker Alpha IR spectrometer equipped with a diffuse reflectance (DRIFTS) accessory with a deuterated triglycine sulfate (DTGS) detector. All measurements are performed in a nitrogen-purged glovebox at room temperature. Samples are prepared by impacting SiNC powders directly from the aerosol phase onto 1" x 1" chips of aluminum coated Si wafer, and transferred via a portable load lock, air free, to the glovebox. A clean aluminum-coated chip is used as a reference. Control measurements on gold and aluminum coated substrates show no coupling effect to the substrate. All spectra are recorded from 400 to 7500 $cm^{-1}$ at 2 $cm^{-1}$ resolution, and averaged over 24 scans. Samples are transferred from the glovebox to a JEOL 6500 SEM equipped with a ThermoFisher Scientific NORAN System 6 EDX. X-rays are collected through a polymer-based window by a crystalline Si detector. Accelerating voltages between 5 and 10 kV are used to maximize dead time while minimizing the damage to the sample. The accelerating voltage is adjusted so that the aluminum layer is not measured, such that the electron beam only probed SiNCs. From these measurements, we estimate the fractional P and O concentration ratio, defined as $X_P = [P]/([P] + [Si]) \times 100\%$ and $X_O = [O]/([O] + [Si]) \times 100\%$, respectively. XRD patterns are recorded from impacted powder on a glass substrate using a Cu K$\alpha$ X-ray source and a Bruker AXS Microdiffractometer. The mean diameter of the NCs is estimated from the line broadening using the Scherrer equation. For low-temperature annealing, a hot plate located inside a nitrogen-purged glovebox is used, and the sample is annealed for 10 min at each temperature. The samples are allowed to cool completely before each measurement. For TEM and STEM studies, samples are prepared by impacting a submonolayer of SiNCs directly onto a copper TEM grid covered with a holey carbon film. The samples are then transferred into a microscope under minimal ambient exposure. Characterization of SiNCs, including high-resolution BF-TEM and HAADF-STEM imaging and EDX is conducted using an FEI Tecnai G2 F-30 (S)TEM with a Schottky field-emission electron gun operated at 300 and 200 kV accelerating voltages, described in detail elsewhere.[32] The microscope is equipped with an EDAX Tecnai 30T/30ST 136−5 EDX Spectrometer.

*Removal of Surface P.* Freshly prepared NC samples produced with varying $X_{PH3}$ are immediately examined with SEM-EDX in order to measure $X_O$ and $X_P$. Other samples prepared under identical conditions are stored in a nitrogen-purged glovebox for 90 h or oxidized under ambient room conditions for 116 h before being examined with SEM-EDX. The oxidized samples are subsequently etched with vapor of hydrofluoric acid in order to remove the Si oxide surface layer and any incorporated P, and then re-examined using SEM-EDX to provide an estimate of $X_P$ in the NC core, as shown in Figure 3c in the main text. In Supporting Information Section S-5, we provide detailed accounting of $X_O$ and $X_P$ during the oxidation and etching processes not included in the main text.

## ■ ASSOCIATED CONTENT

**Ⓢ Supporting Information**

(S-1) Estimate of the LSPR frequency, (S-2) FTIR surface vibrational mode assignments, (S-3) LSPR frequency shift of SiNC films with high dielectric constant solvent addition, (S-4) SiNC twinning upon high $X_{PH3}$, (S-5) Analysis of oxygen and phosphorus concentration during oxidation and etching process. This material is available free of charge via the Internet at http://pubs.acs.org.

## ■ AUTHOR INFORMATION

**Corresponding Author**
*E-mail: kortshagen@umn.edu.

**Author Contributions**
D.J.R. and U.R.K. conceived the project. D.J.R. synthesized the SiNCs and performed IR, XRD, and EDX measurements. J.S.J. performed STEM-EDX measurements and analysis. U.R.K. and K.A.M. supervised the project and contributed to the interpretation of data. All authors discussed results and contributed during manuscript preparation.

**Notes**
The authors declare no competing financial interests.

## ■ ACKNOWLEDGMENTS

## ■ REFERENCES

(1) Kreibig, U.; Vollmer, M. *Optical Properties of Metal Clusters*; Springer: Berlin, 1995.

(2) Rodríguez-Lorenzo, L.; De la Rica, R.; Álvarez-Puebla, R. A.; Liz-Marzán, L. M.; Stevens, M. M. *Nat. Mater.* **2012**, *11*, 604−607.

(3) Kundu, J.; Le, F.; Nordlander, P.; Halas, N. J. *Chem. Phys. Lett.* **2008**, *452*, 115−119.

(4) Jain, P. K.; Huang, X.; El-Sayed, I. H.; El-Sayed, M. A. *Acc. Chem. Res.* **2008**, *41*, 1578−86.

(5) Kelzenberg, M. D.; Boettcher, S. W.; Petykiewicz, J. A.; Turner-Evans, D. B.; Putnam, M. C.; Warren, E. L.; Spurgeon, J. M.; Briggs, R. M.; Lewis, N. S.; Atwater, H. A. *Nat. Mater.* **2010**, *9*, 239−44.

(6) Luther, J. M.; Jain, P. K.; Ewers, T.; Alivisatos, A. P. *Nat. Mater.* **2011**, *10*, 361−6.

(7) Kriegel, I.; Jiang, C.; Rodríguez-Fernández, J.; Schaller, R. D.; Talapin, D. V; Da Como, E.; Feldmann, J. *J. Am. Chem. Soc.* **2012**, *134*, 1583−90.

(8) Manthiram, K.; Alivisatos, A. P. *J. Am. Chem. Soc.* **2012**, *134*, 3995−8.

(9) Li, S. Q.; Guo, P.; Zhang, L.; Zhou, W.; Odom, T. W.; Seideman, T.; Ketterson, J. B.; Chang, R. P. H. *ACS Nano* **2011**, *5*, 9161−9170.

(10) Buonsanti, R.; Llordes, A.; Aloni, S.; Helms, B. A.; Milliron, D. J. *Nano Lett.* **2011**, *11*, 4706−10.

(11) Chou, L.-W.; Shin, N.; Sivaram, S. V; Filler, M. A. *J. Am. Chem. Soc.* **2012**, *134*, 16155−8.

(12) Garcia, G.; Buonsanti, R.; Runnerstrom, E. L.; Mendelsberg, R. J.; Llordes, A.; Anders, A.; Richardson, T. J.; Milliron, D. J. *Nano Lett.* **2011**, *11*, 4415−20.

(13) Ju, L.; Geng, B.; Horng, J.; Girit, C.; Martin, M.; Hao, Z.; Bechtel, H. A.; Liang, X.; Zettl, A.; Shen, Y. R.; Wang, F. *Nat. Nanotechnol.* **2011**, *6*, 630−4.

(14) Chen, H.-T.; Padilla, W. J.; Zide, J. M. O.; Gossard, A. C.; Taylor, A. J.; Averitt, R. D. *Nature* **2006**, *444*, 597−600.

(15) Dalpian, G.; Chelikowsky, J. *Phys. Rev. Lett.* **2006**, *96*, 1−4.

(16) Petropoulos, J. P.; Cristiani, T. R.; Dongmo, P. B.; Zide, J. M. O. *Nanotechnology* **2011**, *22*, 245704.

(17) Erwin, S. C.; Zu, L.; Haftel, M. I.; Efros, A. L.; Kennedy, T. A.; Norris, D. J. *Nature* **2005**, *436*, 91−4.

(18) Fage-Pedersen, J.; Larsen, A.; Mesli, A. *Phys. Rev. B* **2000**, *62*, 10116−10125.

(19) Irmscher, K.; Klose, H.; Maass, K. *J. Phys. C: Solid State Phys.* **1984**, *17*, 6317−6329.

(20) Nobili, D.; Armigliato, A.; Finetti, M.; Solmi, S. *J. Appl. Phys.* **1982**, *53*, 1484.

(21) Pi, X. D.; Gresback, R.; Liptak, R. W.; Campbell, S. A.; Kortshagen, U. R. *Appl. Phys. Lett.* **2008**, *92*, 123102.

(22) Mangolini, L.; Thimsen, E.; Kortshagen, U. R. *Nano Lett.* **2005**, *5*, 655−659.

(23) Stegner, A. R.; Pereira, R. N.; Lechner, R.; Klein, K.; Wiggers, H.; Stutzmann, M.; Brandt, M. S. *Phys. Rev. B* **2009**, *80*, 165326(10 pp.).

(24) Fujii, M.; Mimura, A.; Hayashi, S.; Yamamoto, Y.; Murakami, K. *Phys. Rev. Lett.* **2002**, *89*, 1−4.

(25) Perego, M.; Bonafos, C.; Fanciulli, M. *Nanotechnology* **2010**, *21*, 025602.

(26) Zhang, X.; Brynda, M.; Britt, R. D.; Carroll, E. C.; Larsen, D. S.; Louie, A. Y.; Kauzlarich, S. M. *J. Am. Chem. Soc.* **2007**, *129*, 10668−9.

(27) Schrotter, J.; Cardenas, A.; Smaihi, M.; Hovnanian, N. *J. Sol.-Gel Sci. Technolo.* **1995**, *4*, 195−204.

(28) Glass, J. A.; Wovchko, E. A.; Yates, J. T. *Surf. Sci.* **1996**, *348*, 325−334.

(29) Mangolini, L.; Kortshagen, U. R. *Phys. Rev. E* **2009**, *79*, 26405.

(30) Niesar, S.; Stegner, A. R.; Pereira, R. N.; Hoeb, M.; Wiggers, H.; Brandt, M. S.; Stutzmann, M. *Appl. Phys. Lett.* **2010**, *96*, 193112.

(31) Su, K.-H.; Wei, Q.-H.; Zhang, X.; Mock, J. J.; Smith, D. R.; Schultz, S. *Nano Lett.* **2003**, *3*, 1087−1090.

(32) Behr, M. J.; Mkhoyan, K. A.; Aydil, E. S. *ACS Nano* **2010**, *4*, 5087−94.